Journal of
Synchrotron
Radiation

ISSN 1600-5775

Received 25 January 2013
Accepted 10 July 2013

Soft-X-ray ARPES facility at the ADRESS beamline of the SLS: concepts, technical realisation and scientific applications

V. N. Strocov,* X. Wang, M. Shi, M. Kobayashi, J. Krempasky, C. Hess, T. Schmitt and L. Patthey

Swiss Light Source, Paul Scherrer Institute, CH-5232 Villigen-PSI, Switzerland.
*E-mail: vladimir.strocov@psi.ch

Soft-X-ray angle-resolved photoelectron spectroscopy (ARPES) with photon energies around 1 keV combines the momentum space resolution with increasing probing depth. The concepts and technical realisation of the new soft-X-ray ARPES endstation at the ADRESS beamline of SLS are described. The experimental geometry of the endstation is characterized by grazing X-ray incidence on the sample to increase the photoyield and vertical orientation of the measurement plane. The vacuum chambers adopt a radial layout allowing most efficient sample transfer. High accuracy of the angular resolution is ensured by alignment strategies focused on precise matching of the X-ray beam and optical axis of the analyzer. The high photon flux of up to 10^{13} photons s^{-1} (0.01% bandwidth)$^{-1}$ delivered by the beamline combined with the optimized experimental geometry break through the dramatic loss of the valence band photoexcitation cross section at soft-X-ray energies. ARPES images with energy resolution up to a few tens of meV are typically acquired on the time scale of minutes. A few application examples illustrate the power of our advanced soft-X-ray ARPES instrumentation to explore the electronic structure of bulk crystals with resolution in three-dimensional momentum, access buried heterostructures and study elemental composition of the valence states using resonant excitation.

Keywords: Swiss Light Source; ADRESS beamline; soft-X-ray energy range; angle-resolved photoelectron spectroscopy; electronic structure; bulk sensitivity; three-dimensional momentum; buried heterostructures; resonant photoemission.

1. Introduction

The Swiss Light Source (SLS) is a third-generation synchrotron radiation source situated at the PSI site in Villigen, Switzerland. Its storage ring operates at 2.4 GeV electron energy with a current of 400 mA.

The ADRESS (ADvanced RESonant Spectroscopy) undulator beamline is installed in the X03M middle straight section of the SLS. It is designed for experiments with resonant inelastic X-ray scattering (RIXS) and angle-resolved photoelectron spectroscopy (ARPES) in the soft-X-ray range with high energy resolution. The RIXS endstation (Schmitt *et al.*, 2013) has been open for users since autumn 2007, and the ARPES endstation since spring 2011. The beamline is described in detail by Strocov *et al.* (2010). Briefly, it delivers soft-X-ray radiation with variable polarizations in the range of photon energies $h\nu$ from 300 to 1600 eV. The key beamline performance feature is the high photon flux topping up 10^{13} photons s^{-1} (0.01% bandwidth)$^{-1}$ near 1 keV. The spot size on the sample in the ARPES endstation is 10 µm (vertical) × 73.6 µm (horizontal).

The soft-X-ray ARPES (SX-ARPES) endstation is intended for investigations of the electronic structure, correlation and resonance effects in crystalline solids with resolution in three-dimensional momentum **k** (see, for example, Hüfner, 1996). Pioneered at SPring-8 (Sekiyama *et al.*, 2004; Suga *et al.*, 2004), soft-X-ray ARPES (SX-ARPES) exploits the $h\nu$ range around 1 keV. It features a few fundamental advantages compared with the conventional VUV-ARPES in the $h\nu$ range around 100 eV:

(i) Increase of the photoelectron kinetic energy E_k results in increase of the photoelectron attenuation length λ by a factor of two to five compared with the conventional ARPES as described, in the first approximation, by the 'universal curve' (see, for example, Powell *et al.*, 1999). This enhances the bulk sensitivity of the ARPES experiment as well as enabling experimental studies of buried interfaces and heterostructures.

(ii) Sharp definition of the surface-perpendicular momentum $k_\perp$ which enables accurate investigations of electronic structure in three-dimensional materials (Strocov *et al.*, 2012). This has two aspects. (*a*) The final-state confinement within λ results, by the Heisenberg uncertainty principle, in intrinsic broadening of its $k_\perp$ defined by $\Delta k_\perp = \lambda^{-1}$. The increase of λ results therefore in improvement of the intrinsic $k_\perp$ resolution (Strocov, 2003). (*b*) The final-state dispersion becomes free-electron-like which allows accurate determination of the $k_\perp$ value distorted during the photoelectron escape into vacuum.

(iii) The photoemission matrix elements reduce basically to atomic cross sections (Solterbeck *et al.*, 1997) varying only smoothly under variations of energy and **k**. The concomitant regularity of the ARPES response significantly simplifies the data analysis.

The main difficulty of SX-ARPES, until now severely impeding the use of this technique, is that the photoexcitation cross section Ω of valence states reduces compared with the VUV energy range by typically two to three orders of magnitude. This is illustrated in Fig. 1 which shows Ω as a function of $h\nu$ for the Cu 3*d*, Fe 3*d*, O 2*p* and As 4*p* states (relevant for the cuprate and pnictide superconductors). Such a dramatic signal loss (note the logarithmic scale) has to be compensated by a high flux of incoming photons, which requires advanced synchrotron radiation sources and beamline instrumentation. Another difficulty is that the soft-X-ray photoelectron wavelengths become comparable with the thermal motion amplitudes. The electron–phonon scattering then destroys the coherent spectral structures through their Debye–Waller amplitude reduction and broadening, and piling up an incoherent background reflecting **k**-integrated density of states (Venturini *et al.*, 2008; Gray *et al.*, 2011). Low sample temperatures are therefore of paramount importance for SX-ARPES.

Here, we describe the concepts and technical realisation of the new SX-ARPES endstation installed at the ADRESS beamline. We illustrate its performance with a few pilot scientific cases which highlight the benefits of SX-ARPES, in particular in application to three-dimensional materials and buried heterostructures.

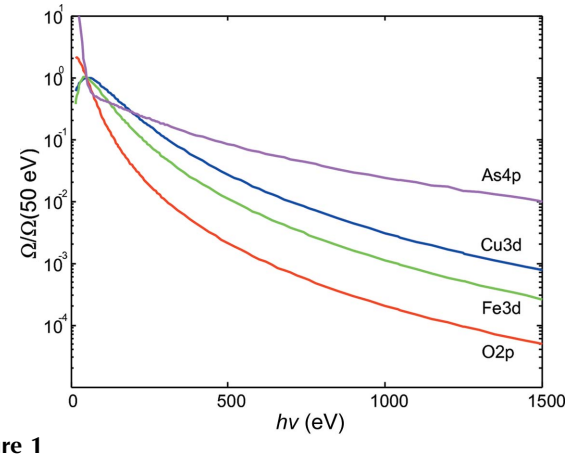

Figure 1
Photoexcitation cross sections Ω of the Cu 3*d*, Fe 3*d*, O 2*p* and As 4*p* states as a function of $h\nu$ (Yeh & Lindau, 1985) normalized to their values at 50 eV. The dramatic loss of Ω with $h\nu$ requires high photon flux for the SX-ARPES experiment.

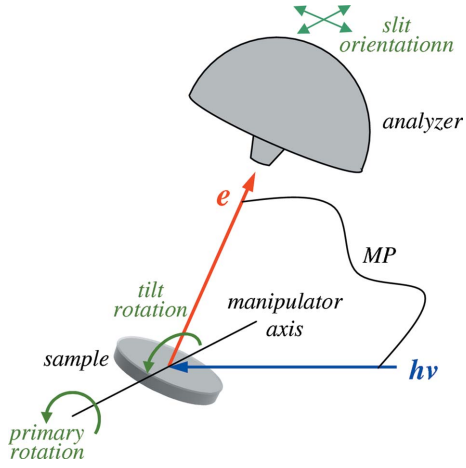

Figure 2
Sketch of the experimental geometry. Its main features are the grazing X-ray incidence, vertical measurement plane (MP) and horizontal manipulator axis.

2. Concepts and geometry

The geometry of our SX-ARPES experiment (corresponding to the normal emission) is sketched in Fig. 2. The X-rays come to the sample at a grazing-incidence angle of 20°. The analyzer lens axis is perpendicular to the sample surface. The incident beam and analyzer lens form the vertical measurement plane (MP). The manipulator is mounted in the horizontal axis orientation and delivers the primary and tilt rotations.

This less conventional experimental geometry was dictated by the following concepts.

2.1. Incidence angle

The optimal X-ray incidence angle is determined by maximization of the electromagnetic field absorption within the relatively small λ. Following Henke's seminal ideas (Henke, 1972), the following formula can be derived for the normal-emission photocurrent $I_{\rm PE}$ as a function of the X-ray grazing-incidence angle α,

$$I_{\rm PE}(\alpha) \propto [1 - R(\alpha)]\,\frac{\lambda}{d(\alpha) + \lambda}, \qquad (1)$$

where $R(\alpha)$ is the reflection coefficient of X-rays and $d(\alpha)$ their penetration depth (for details see Strocov, 2013). We used this expression to calculate $I_{\rm PE}(\alpha)$ from valence states of two common materials, Cu and GaAs, at the two ends of our $h\nu$ range. The numerical values of R and $d(\alpha)$ were taken from the X-ray database (Henke *et al.*, 1993) and those of λ as the inelastic mean free path from Powell *et al.* (1999) as compiled in the NIST Standard Reference Database 82 (available at http://www.nist.gov/srd/nist82.cfm) and calculated with the TPP-2M formula. The results are shown in Fig. 3.

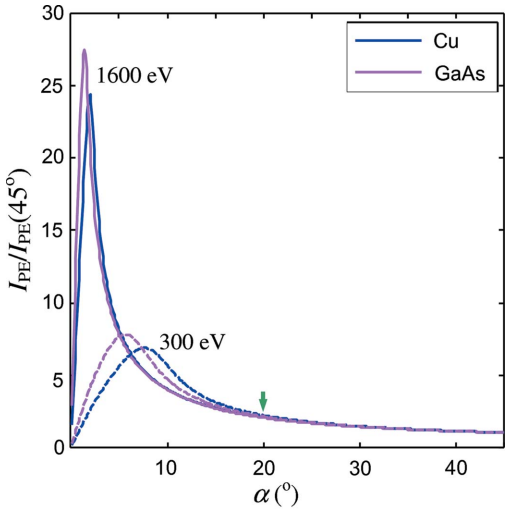

Figure 3
Normal-emission photoelectron intensity calculated for Cu and GaAs as a function of grazing X-ray incidence angle at $h\nu = 300$ (dashed lines) and 1600 eV (solid lines). The intensities are normalized to their value at 45°. The actual working point is indicated (arrow).

The general trends appear fairly material-independent. When going towards more grazing angles, $I_{PE}(\alpha)$ first gradually decreases proportional to $(\sin\alpha)^{-1}$ and then sharply increases near the critical reflection angle α_c when the electromagnetic field concentrates in the near-surface region where the photoelectrons come from [for a physical picture of the interplay of the X-ray reflection, penetration and photoelectron escape, see Strocov (2013)]. We note that our results radically differ from the previous works based on Henke's formalism (for a review see Fadley *et al.*, 2003) whose $I_{PE}(\alpha)$ showed a plateau in the region of less-grazing angles and only a moderate increase around α_c. The difference comes because our formalism (1) assumes that the X-ray footprint on the sample always stays within the analyzer field of view, the situation typical of the nowadays synchrotron instrumentation delivering a beam focused to a few micrometers. Henke's formula (Henke, 1972) assumed the opposite situation which multiplied I_{PE} by the $\sin\alpha$ factor.

The I_{PE} peak in Fig. 3 identifying the optimal α appears around 8° for 300 eV and 2° for 1600 eV, obviously going more grazing with energy. This suggests an experimental geometry with $\alpha = 8^{\circ}$ corresponding to the low-energy end of our $h\nu$ range. However, technical restriction of our manipulator have forced us to relax α to 20°. Such a less-aggressive angle also (i) helps reduce the vibration sensitivity; and (ii) allows more room for variation of α to change the emission angle without dramatic intensity effects. Anyway, Fig. 3 shows that the gain of $I_{PE}(\alpha)$ with our $\alpha = 20^{\circ}$ compared with $\alpha = 45^{\circ}$ used in the conventional ARPES set-ups is a factor of more than two throughout our energy range.

2.2. Manipulator and MP orientation

Going to grazing incidence blows up the X-ray footprint on the sample proportionally to $(\sin\alpha)^{-1}$. This may become a problem for ARPES measurements, because the photoelectron source extension along the analyzer slit above a characteristic size of ~100 µm starts to deteriorate the angular resolution. Furthermore, larger footprints will also complicate experiments on inhomogeneous and mosaic samples. The focused X-ray beam delivered by a synchrotron source has an elliptical shape with the horizontal size S_H much larger than the vertical one S_V. Therefore, the sample should be inclined to the grazing incidence by rotation around the horizontal axis to blow up the smaller S_V rather than the larger S_H. This dictates the horizontal manipulator axis orientation perpendicular to the MP.

S_V is defined by the demagnification D of the exit slit s and aberration limit S_A of the refocusing optics as $S_V = [(sD)^2 + S_A^2]^{1/2}$. In our case with $D = 0.305$ and $S_A = 10$ µm, a realistic slit opening $s = 20$ µm defines the vertical X-ray footprint on the sample $S_V/\sin\alpha$ more than twice smaller than $S_H = 73.6$ µm. This excludes any effect of the grazing incidence on the angular or spatial resolution of the experiment. In future we plan to further reduce both horizontal and vertical beam size using ellipsoidal refocusing optics with stronger demagnification.

2.3. Analyzer rotatability

The analyzer can be turned around the lens axis to orient the slit either parallel or perpendicular to the MP. We mostly use the parallel orientation, which enables the symmetries of the valence states to be explored by switching the incident light polarization from the linear vertical to horizontal to excite either symmetric or antisymmetric states. With this orientation we sample **k**-space by changing the emission angle through the tilt rotation of the manipulator. The perpendicular slit orientation allows us to sample **k**-space by the primary manipulator rotation having a larger range.

Finally, we note that in the soft-X-ray energy range the navigation in **k**-space based on the momentum conservation should be corrected for the photon momentum $p_{ph} = 2\pi/\lambda_{ph}$, λ_{ph} being the photon wavelength, which becomes comparable with the Brillouin zone (BZ) dimensions (see, for example, Venturini *et al.*, 2008). The correction formulae tailored to our experimental geometry are compiled in Appendix *A*.

3. Technical realisation

3.1. Endstation layout

A sketch of our experimental set-up is shown in Fig. 4. The X-ray beam is focused on the sample with the toroidal refocusing mirror (RM) driven by high-precision hexapod mechanics (Strocov *et al.*, 2010). The endstation consists of the following vacuum chambers:

(i) Analysis chamber (AC) where the photoelectron analyzer is installed. The absence of any other analytical tools there defeats the risks that the AC has to be vented for their reparations.

(ii) Transfer chamber (TC) which is a hub to distribute samples between all other chambers. It is equipped with a sample park. Sample cleavages on the manipulator cooled to

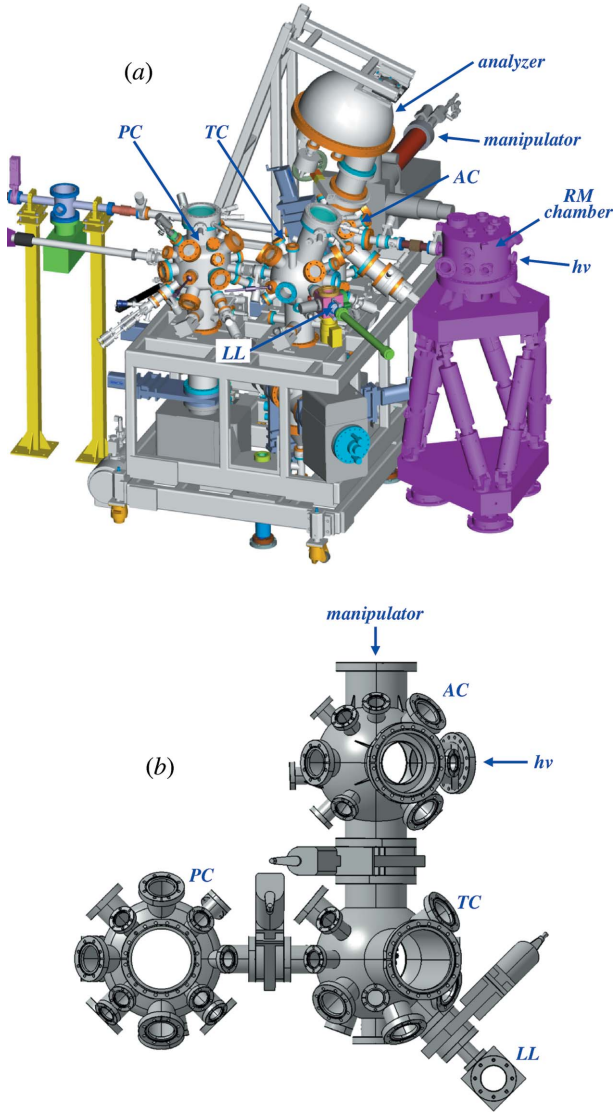

Figure 4
Layout of the SX-ARPES endstation in a perspective view (*a*) and of its vacuum chambers in a top view (*b*). An important feature of the endstation is the radial arrangement of the analysis chamber (AC), preparation chamber (PC) and load lock (LL) around the transfer chamber (TC).

low temperature are also performed in the TC. A LEED system allows control of the surface crystallinity. The bottom of the TC is conically reduced to a miniature vessel which is separated by a gate valve and serves as a bin for the cleavage products and dropped samples. This allows us to rescue the content of the bin without breaking vacuum in the TC.

(iii) Preparation chamber (PC) provides sample preparation facilities such as gas exposure, ion bombardment, heating up to 1473 K, and quartz balance controlled deposition of thin films from e-beam and effusion sources with the possibility to accept user sources. The PC is equipped with another LEED system.

(iv) Load lock (LL) for the sample introduction. It has an option for *in situ* transfer of samples from a vacuum suitcase. In particular, we use this option to introduce the samples prepared in another in-house set-up for pulsed laser deposition (PLD) which we routinely use to prepare samples of correlated transition metal oxides and their heterostructures.

In practice, the predominant majority of our samples can be prepared by *in situ* cleavage [layered materials, high-temperature superconductors (HTSCs), some oxide and perovskite systems] or do not require surface preparation at all (such as protected surfaces or less reactive PLD grown oxide systems). For these samples the radial layout of the vacuum chambers around the TC is particularly advantageous because (*a*) only one transfer operation is required for the samples on their way to the AC, which significantly increases the endstation throughput, and (*b*) these samples do not pass the PC, avoiding any risk of contamination by residuals of the surface preparations.

The endstation platform is mounted on retractable wheels which gives us the possibility of removing the endstation from the beamline in case of a serious reparation or to accept a user endstation. The platform is fixed in the beamline on metal studs in the SLS floor using a point-V-flat positioning system which ensures a reproducibility of better than ± 20 µm.

3.2. Manipulator

The endstation is equipped with a CARVING manipulator (Patthey, 2010), the commercial version available from SPECS GmbH. The manipulator delivers three translational degrees of freedom (DOFs) with an accuracy of 10 µm and three mechanically decoupled angular DOFs (primary, tilt and azimuthal rotations) with an accuracy of 0.05°. The operational range of the primary rotation is 270°, of the tilt $\pm 30°$ and azimuth $\pm 180°$. The manipulator is equipped with a He flow cryostat with thermal shielding which allows working temperatures down to 10.5 K as measured on the clamps embracing the sample. Such low sample temperatures are sufficient to quench the destructive effects of electron–phonon scattering even for soft materials with low Debye temperatures.

The sample holders adopt the standard SLS design to ensure compatibility with other experimental stations at SLS including two PLD set-ups and the VUV-ARPES station at the SIS beamline. The standard holders are made of oxygen-free Cu and allow efficient cooling down of the samples to He temperatures. Modifications of these holders carry an integrated knife-anvil cleavage system (Månsson *et al.*, 2007). Another type of sample holder is made of Mo and carries electron bombardment assemblies to heat up the samples to 1473 K.

3.3. Analyzer

The endstation uses the angle-multiplexing photoelectron analyzer PHOIBOS-150 from SPECS GmbH. The basic operational principles of these analyzers are described by Mårtensson *et al.* (1994) and Wannberg (2009). The ultimate energy resolution of our analyzer is better than 5 meV, which is not critical in our case because the combined resolution is limited by the beamline anyway. The angular resolution $\delta\theta$ of

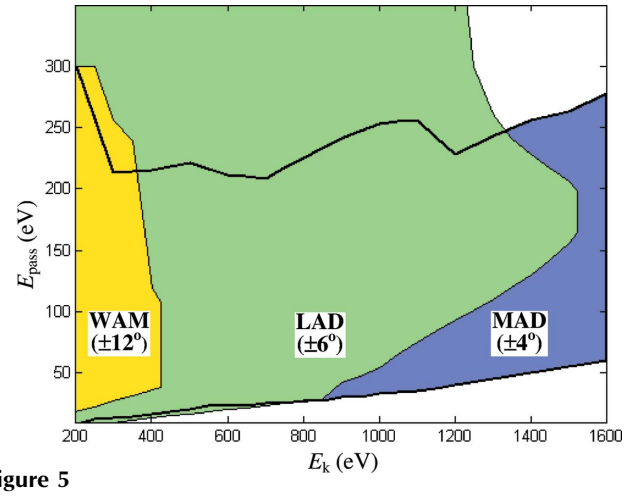

Figure 5
Operational regions of the three AR modes of the PHOIBOS-150 analyzer (WAM, LAD and MAD).

the analyzer is about 0.07° FWHM, which is in fact much better than planarity errors of typical cleaved surfaces. We note that high angular resolution is particularly important for the SX-ARPES experiments because the angular errors $\delta\theta$, translated into $K_{\parallel}$ according to the well known expression $\delta K_{\parallel} = 0.5124(E_k)^{1/2}\sin\delta\theta$, are magnified by high kinetic energies E_k. At 1 keV, our $\delta\theta$ corresponds to $\delta K_{\parallel} \simeq 0.02$ Å^{-1} or about 2% of the typical BZ dimensions.

The PHOIBOS-150 analyzer offers three angle-resolving (AR) modes whose ranges of accurate angular scale are ±12° (wide-angle mode, WAM), ±6° (low angular dispersion, LAD) and ±4° (medium angular dispersion, MAD). Fig. 5 shows the operational regions of these modes in coordinates of E_k and pass energy E_{pass}. The larger their angular acceptance, the smaller their operational E_k range. The low E_{pass} border is the maximal retarding ratio E_k/E_{pass} delivering accurate angular scale.

The analyzer can acquire the data either in the fixed mode (the central E_k is fixed and the data are acquired simultaneously through the whole MCP energy window of ∼12% of E_k) or in the sweep mode (the central E_k sweeps through a certain energy range). Theoretically, in the ideal case of infinitely fast data transfer, the acquisition in the fixed mode is faster by a factor of two compared with that in the sweep mode within the same energy window. In practice, the data transfer slows down the sweep mode even more. Therefore, we normally use the fixed mode. Operation of the PHOIBOS-150 in this mode is possible owing to homogeneous illumination of the MCP and the absence of any mesh in front of it.

Finally, we should mention that all analyzers using MCPs suffer from stray intensity coming from photoelectrons which hit the areas between the MCP pores (see, for example, Taylor *et al.*, 1983). These electrons create a cloud of secondary electrons which spread over the MCP surface to create the stray signal through all pores in the nearby region. This effect is illustrated in Fig. 6 which shows an image formed by a mask of five slits inserted at the hemisphere exit plane (*a*) and the corresponding angle-integrated spectrum (*b*). The charge spread effect is seen as profound feet of the peaks. A common

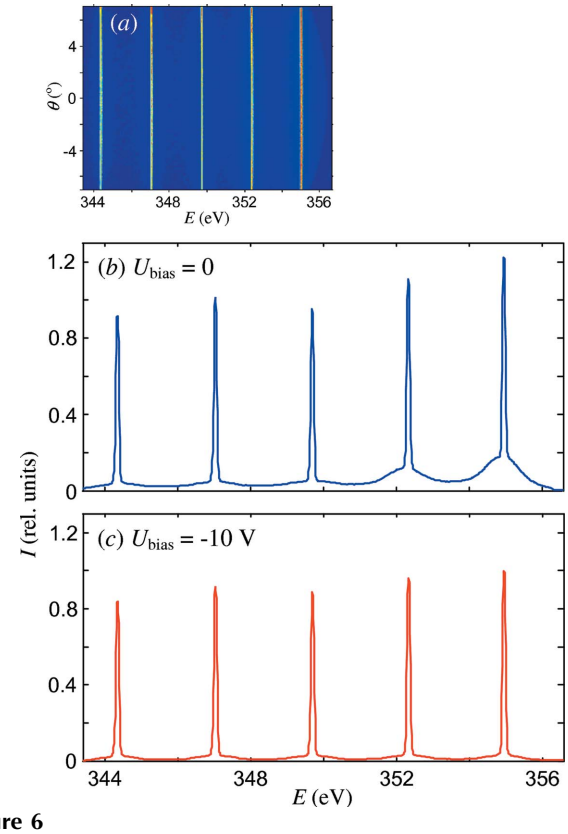

Figure 6
Typical image produced by the slit mask inserted at the hemisphere exit plane (*a*) and the corresponding angle-integrated spectra, with the MCP biased by U_{bias} equal to zero (*b*) and −10 V (*b*) (LAD mode, E_k = 350 eV, E_p = 100 eV). The bias dramatically reduces the feet of the peaks formed by the charge spread.

method to suppress this is to apply larger event discrimination levels, but this results in non-linear response at larger intensities. Our method was to apply to the MCP surface a slight retarding bias U_{bias} (Maehl, 2012). Its optimal value, almost completely quenching the stray intensity but still not inducing any significant signal reduction or MCP illumination inhomogeneity, was found to be around 10% of E_p. Fig. 6(*c*) shows that the optimal U_{bias} almost completely removes the stray intensity at negligible decrease of the signal itself. A slight effect of this U_{bias} on the angular scale can be corrected from calibration measurements with the slit array (see below). We note that in contrast to the event discrimination method this solution ensures the intensity response linearity.

4. Software

In the ARPES experiment, one normally performs serial data acquisitions under variations of certain beamline, manipulator and analyzer parameters. Our software for this purpose is *SmartGUI* implemented in MATLAB. This programming environment was dictated by a variety of its built-in data-processing functions and availability of free libraries for the EPICS channel access to control the beamline. To control the analyzer voltages and acquisition of the CCD images, *SmartGUI* connects to the software *SpecsLab2* coming

with the PHOIBOS-150 analyzer. The acquired data are saved in the HDF5 format, which allows multidimensional data blocks supplemented by descriptive attributes such as the beamline and manipulator parameters. Another advantage of this format is its support by different data analysis platforms including MATLAB and IGOR Pro.

The minimalistic and intuitive table-like interface of *SmartGUI* is shown in Fig. 7(*a*). Each row represents a data acquisition run with its parameters specified in the groups File (data file name and comment), Beamline (polarization, $h\nu$ and exit slit), Analyzer (angular mode, photoelectron kinetic energy $E_{\rm k}$ and pass energy $E_{\rm p}$) and Manipulator (primary, tilt and azimuthal angle). The rows can be copied, pasted and cleared. What makes this GUI 'smart' is that the inputs of $h\nu$ and manipulator angles can be vectorized using the standard MATLAB notation $x_{\rm start}{:}\Delta x{:}x_{\rm end}$. In our example in Fig. 7(*a*) this vectorized parameter (VP) is $h\nu$ for the first three runs and the tilt angle for the last three. The vectorization automatically transforms the run to a series of acquisitions upon scanning through the VP values. The two-dimensional images of ARPES intensity as a function of the angle and energy, produced in each acquisition, are then stacked in one single three-dimensional data block as a function of the angle, energy and VP, which is then saved on the hard disk. The $E_{\rm k}$ vectorization has a different functionality: scalar input runs acquisition in the fixed mode, and vector input in the energy sweep mode.

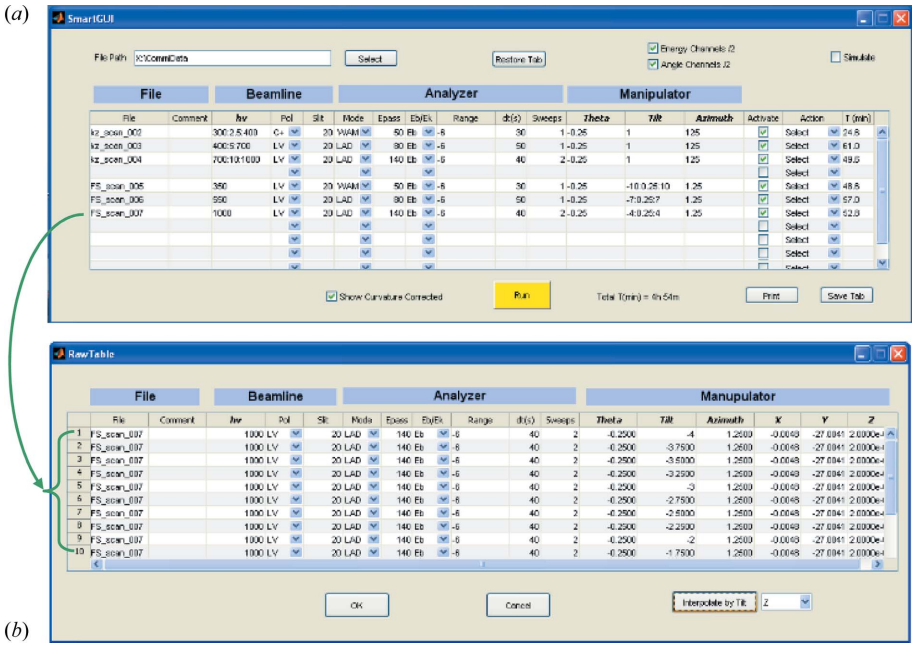

Figure 7
Vectorized user interface of *SmartGUI* (*a*) and its last row expanded in the raw table of separate data acquisitions (*b*).

On the lower level, *SmartGUI* expands the above vectorized table to create a raw table, shown in Fig. 7(*b*), where each line corresponds to a separate acquisition with scalar parameters. The manipulator translational coordinates are also included on this level. There is an option to manually edit all raw table inputs. A generic Interpolate tool also available on this level allows setting of each raw table parameter to automatically track the VP. This functionality is useful, for example, to set translational coordinates to track the rotation angle. Another common situation is measurement of $k_\perp$ dependences away from the normal emission, when the emission angle should track $h\nu$ to keep $\mathbf{k}_\parallel$ constant.

5. Alignment

The alignment procedure aims to bring the focused X-ray beam to the exact focal point of the analyzer. With our experimental geometry in Fig. 2, we performed the alignment in three steps:

(i) Focusing of the X-ray beam. For this purpose we used a fluorescent YAG crystal installed at the sample position, with the X-ray spot monitored using a 1 Mpixel CCD camera fitted with a telephoto objective. The crystal was placed at the nominal focal plane of the analyzer, for the PHOIBOS-150 at 40 mm from the lens, and centered on the analyzer lens axis as marked with a laser mounted at the back of the lens and shooting through it. Then we used the RM roll to steer the beam vertically towards the height of the analyzer axis on the sample (the roll adjustment has only a minor effect on focusing) and focused the beam with the RM pitch (which is associated with horizontal displacement of the beam).

(ii) Determination of the electrostatic focal axis (EFA) of the analyzer. Imperfections in alignment of elements in the analyzer electron optics, however small, normally result in a deviation of the EFA from the above geometrical lens axis up to a few hundreds of micrometers. We found the EFA by steering the RM in roll and pitch until the X-ray beam matched the EFA (the methods to identify the matching are described below).

(iii) Bringing the EFA to the focal position of the X-ray beam. This is achieved by mechanical adjustment of the whole endstation, carrying the fixed analyzer, according to the difference between the determined positions of the EFA and focused X-ray beam on the sample. Remnant misfits of the order of a few tens of micrometers can be compensated by fine tuning of the RM, with the limits of tunability without notable defocusing being in our case about ± 25 µrad for the pitch and ± 2 mrad for the roll.

We will now comment on the methods to control the beam/EFA matching. Whereas for the imaging (magnification) and transmission modes of the ARPES analyzer this is trivial, we will concentrate on the AR modes. In the direction perpendicular to the analyzer slit, the matching is simply the maximal photoemission intensity. In the direction parallel to the slit, the matching is connected to the angular scale. To investigate this

connection, we used a slit array on top of the sample to define a pattern of emission angles in steps of 1°. Fig. 8(*a*) shows the corresponding ARPES images of homogeneous secondary-electron background, measured at the exact matching and with a mismatch of ±1 mm. The latter results in displacement and skewing of the angular scale. Therefore, the criterion of the beam/EFA matching is the straight angular scale. Our observations of these non-trivial effects were later confirmed by ray-tracing calculations (Maehl, 2012). For our analyzer, we found that the accurate angular scale is ensured as long as the mismatch does not exceed ±50 µm. We note that this naturally defines the maximal spot size to stay with the best angular resolution, which is exactly the figure of 100 µm discussed above. In routine experiments without the slit array, the beam/EFA matching can be conveniently controlled with the iris built into the PHOIBOS-150 lens to vary the angular acceptance. This is illustrated in Fig. 8(*b*) which shows AR images of secondary-electron background measured with reduced iris. Under the beam/EFA mismatch, these bands of illumination on the detector displace and skew exactly as the slit array images.

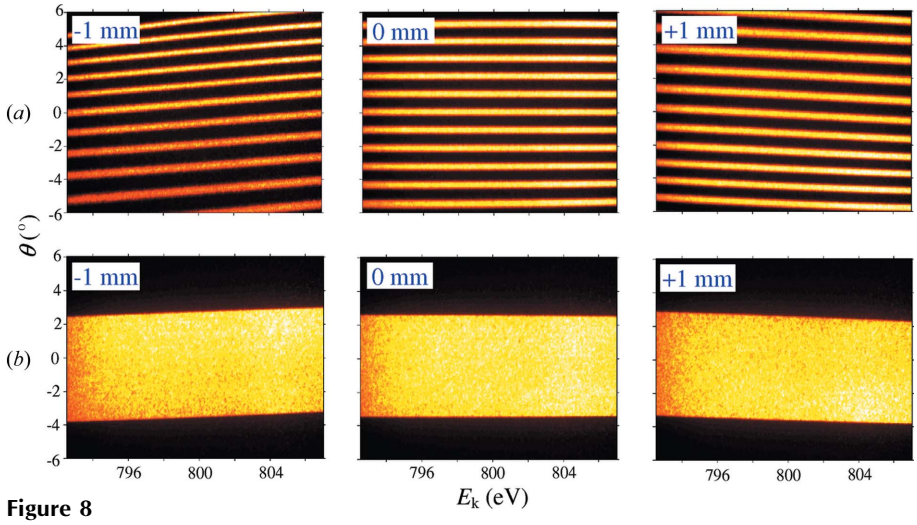

Figure 8
Effect of the analyzer focal axis and incident beam mismatch of ±1 mm in the slit-parallel direction (LAD mode, E_k = 800 eV, E_p = 120 eV): (*a*) angle-resolved image of the slit array defining angular steps of 1°, and (*b*) illumination band produced by restricted analyzer iris. The misfit results in displacement and skewing of these images.

Switching between the analyzer modes slightly displaces the EFA, which again traces back to the alignment of elements in the analyzer electron optics. For our PHOIBOS-150 the displacements are up to 300 µm. These values are still small enough and can be compensated by fine adjustments of the RM without notable defocusing of the X-ray beam. With our high-precision RM mechanics, these adjustments are fully reproducible and, once determined, in routine experiments can be automatically switched with the analyzer modes. More problematic is the analyzer rotation to change the slit orientation, owing to wobble of the rotational mechanics and the EFA. In our case the latter displaces along the sample around 1.5 mm. The required RM adjustments, especially in pitch, would then notably defocus the X-ray beam. Therefore, to achieve the highest experimental accuracy, the slit orientation changes should be accompanied by mechanical re-adjustment of the endstation.

In practical experiments, certain variations of the sample height displace the X-ray footprint away from the EFA. To recover their exact matching, the sample is translated along the EFA. As discussed above, in the AR modes the matching is controlled through the signal intensity (if the analyzer slit is perpendicular to the MP) or using the iris (parallel to the MP). We note that commonly accepted in the ARPES experimental practice is to align the sample height using magnification or transmission analyzer modes, and then perform measurements in AR modes. However, this cannot be considered accurate because the EFA displacement between the modes can compromise the angular scale accuracy.

The achieved performance of our set-up in the AR modes is illustrated in Fig. 9(*a*) with typical slit array images in all three AR modes of our PHOIBOS-150. The images demonstrate an

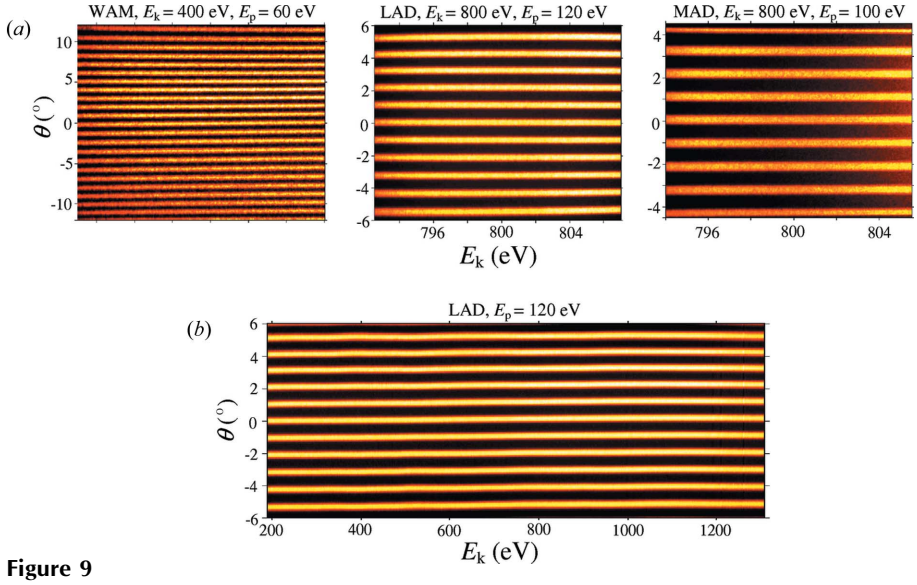

Figure 9
Typical angle-resolved slit array images acquired in (*a*) the fixed analyzer mode and (*b*) the scanning mode in a wide range of E_k (with the intensity normalized to remove the Auger and core level peaks). The acquisition parameters are indicated on the images. The angular scale is fairly accurate and practically independent of E_k.

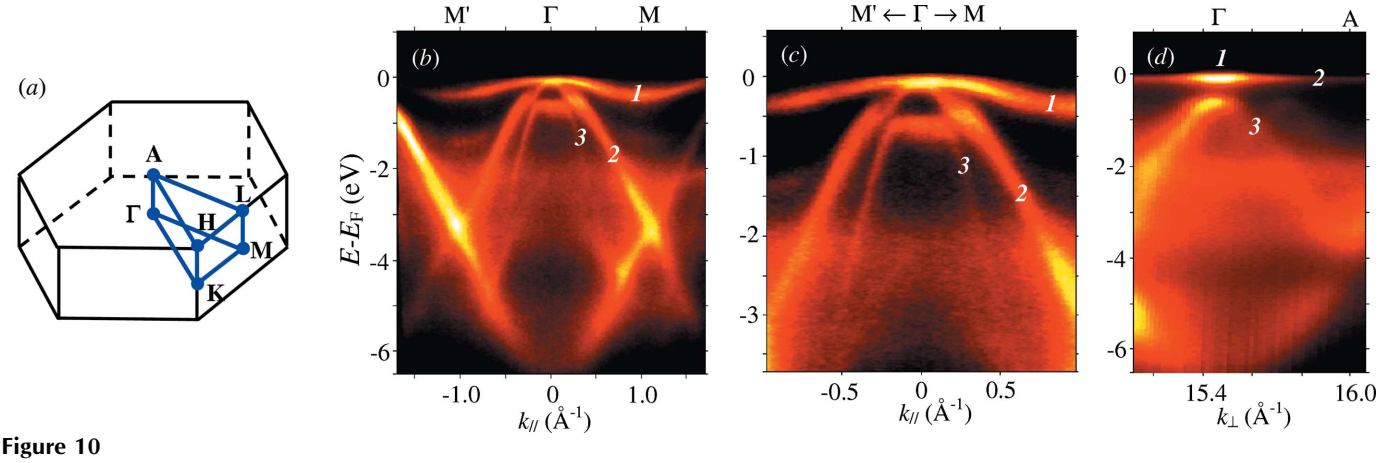

Figure 10
(*a*) BZ of VSe_2 with its main symmetry lines, and (*c*)–(*d*) experimental ARPES intensity: (*b*) $I(E, k_\parallel)$ image along the M′ΓM line measured at $h\nu$ = 885 eV and (*c*) its high-resolution blow-up; (*d*) $I(E, k_\perp)$ map along the ΓA line where $k_\perp$ is varied by scanning $h\nu$. The V 3*d*, Se $4p^*_{xy}$ and Se $4p^*_z$ bands are marked by 1, 2 and 3, respectively. Despite high $h\nu$, the experimental results show excellent statistics and contrast (Strocov *et al.*, 2012).

undistorted and fairly accurate angular scale. Fig. 9(*b*) shows typical results acquired with E_k scanning a wide energy range from 200 to 1300 eV. The angular scale is practically energy independent. We could note certain distortions only at very large E_k/E_{pass} values. However, a closer look on all images in Fig. 9 reveals a tiny asymmetry of the angular dispersion, partly connected with biasing of the MCP in our PHOIBOS-150. Extending the standard angle correction algorithm of the SPECS analyzers, we routinely correct all these distortions at the post-processing stage by re-defining the angular scale of the acquired images with a third-order polynomial correction,

$$\theta(X, Y) = \sum_{i=1}^{3} \sum_{j=0}^{2} a_{ij} (X - X_0)^i (Y - Y_0)^j, \qquad (2)$$

depending on the pixel position X in the angular direction and Y in the energy direction relative to the image center (X_0, Y_0). The coefficients a_{ij} depending on the particular AR mode and E_k/E_{pass} are reproducible and have been determined by linear fitting of (2) over a series of experimental slit array images.

6. Application examples

6.1. Looking three-dimensional: electronic structure of VSe_2

Our first example illustrates the ability of SX-ARPES to resolve electronic structure in three-dimensional **k**-space in application to VSe_2. The chalcogen–metal–chalcogen layered structure of this material results in its quasi-two-dimensional properties (Woolley & Wexler, 1977). However, the out-of-plane Se p_z states retain pronounced three-dimensional character characterized by their $k_\perp$ dispersion range of a few eV. Studies of three-dimensional electronic structure of such materials with VUV-ARPES are difficult because of non-free-electron character and large intrinsic $k_\perp$ broadening of their low-energy final states (see Strocov *et al.*, 1997, 2006, and references therein).

The experiments used *s*-polarization of incident X-rays, which normally delivers intensity a few times higher than *p*-polarization. The analyzer slit was oriented perpendicular to the MP. The sample temperature was 10.7 K. Variations of E_k, emission angle θ and $h\nu$ were rendered to variations of the three-dimensional **k**-vector taking into account $\mathbf{p}_{ph}$ (see Appendix *A*) and assuming free-electron final states with an inner potential V_0 = 7.5 eV.

Fig. 10(*a*) sketches the BZ of VSe_2. Fig. 10(*b*) shows the experimental ARPES image $I(E, k_\parallel)$ along the M′ΓM line measured with $h\nu$ = 885 eV. The combined (beamline and spectrometer) energy resolution ΔE was set here to ∼120 meV and the acquisition time was only 7 min. Fig. 10(*c*) shows the region near the Fermi level E_F measured with ΔE sharpened to ∼70 meV and acquisition time increased to 40 min. Fig. 10(*d*) presents the $I(E, k_\perp)$ map along the perpendicular ΓA direction acquired with $h\nu$ varying from 845 to 960 eV.

The ARPES images clearly show the V 3*d* bands near E_F forming the Fermi surface (FS), as well as the Se 4*p* ones deeper in the valence band. Two points must be noted:

(i) Excellent statistics of the experimental data is remarkable in view of the valence band Ω dramatically reducing in the soft-X-ray energy range. In the atomic wavefunctions approximation, Ω drops by a factor of ∼1800 for the V 3*d* states and ∼34 for the Se 4*p* states compared with a typical VUV-ARPES energy of 50 eV (Yeh & Lindau, 1985). Evidently, the key factor to break through the drop of Ω has been the high flux delivered by the ADRESS beamline.

(ii) Without any image enhancement, the spectral structures demonstrate profound amplitudes and angular contrast as well as the absence of any significant **k**-integrated background. Obviously, our low working temperatures are sufficient to quench the destructive electron–phonon interaction effects even for VSe_2 having quite a low Debye temperature of 220 K.

Fig. 11(*a*) sketches the FS of VSe_2 (Woolley & Wexler, 1977). Reliable control over $k_\perp$ in our experiment has allowed us to slice the FS in different planes. Fig. 11(*b*) shows the ΓALM slice acquired under variations of $h\nu$ from 845 to 960 eV to span $k_\perp$. Figs. 11(*c*)–11(*e*) present the ΓKM ($k_\perp$ = 0) and AHL ($k_\perp$ = ΓA) slices as well as the slice at half of the BZ height ($k_\perp$ = ΓA/2) acquired under variations of θ to span $\mathbf{k}_\parallel$.

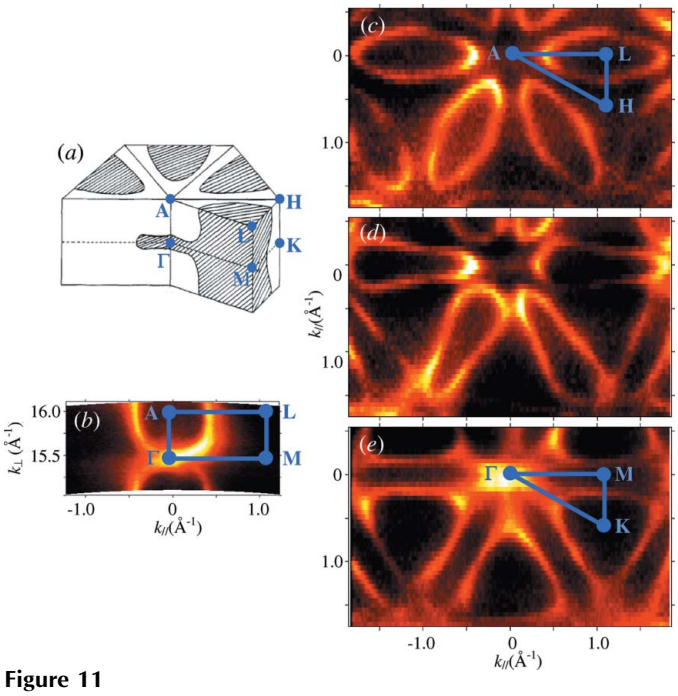

Figure 11
(*a*) Sketch of the FS of VSe_2, and (*b*)–(*e*) experimental FS slices in the (*b*) ΓALM plane of the BZ, (*c*)–(*e*) ΓKM central plane ($h\nu$ = 885 eV), at half of the BZ height (915 eV) and ALH face plane (945 eV), respectively. The maps show a textbook clarity without any image structure enhancement or symmetrization (Strocov *et al.*, 2012).

Each map was acquired within ∼4 h. We note that due to high E_k the variations of $k_\perp$ with $\mathbf{k}_\parallel$ are small compared with the VUV-ARPES energies.

The FS topology with its characteristic sixfold symmetry in the BZ symmetry planes and threefold symmetry in the BZ interior is extremely clear in the experimental maps. Its sharpness in **k**-space is much superior to the previous VUV-ARPES results (Terashima *et al.*, 2003).

We note that our experimental electronic structure of VSe_2 shows a textbook clarity, which identifies an excellent definition of $k_\perp$ achieved by virtue of free-electron final states and their small $k_\perp$ broadening as well as smooth matrix elements delivered by soft-X-ray photon energies. A detailed account of these results, in particular analysis of three-dimensional warping of the FS to form exotic three-dimensional charge density waves, is given by Strocov *et al.* (2012).

6.2. Looking deep: electronic structure of GaAs behind a protective layer

Our second example illustrates the penetrating ability of SX-ARPES achieved by virtue of the increasing photoelectron λ. Our samples were p-doped GaAs(100) thin films grown by molecular beam epitaxy. They were protected from oxidation and contamination from air by deposition of a capping layer of amorphous As with a thickness of 5–10 Å. These GaAs/As samples were introduced into the analysis chamber directly from air without any surface treatment. The measurements were performed with the analyzer slit oriented in the MP which allowed us to investigate the symmetries of the valence states.

Fig. 12 shows the experimental ARPES images acquired on our GaAs/As samples along the ΓKX direction with increasing $h\nu$. The combined ΔE in these measurements, not critical on resolution, was set to ∼200 meV, and the acquisition time was 5 min per image. The indicated $h\nu$ values were chosen to keep $k_\perp$ in the Γ-point based on the free-electron dispersion of the final states with an empirical V_{000} value of 10 eV. Here we used circularly polarized incident X-rays.

The low-energy ARPES image is dominated by a non-dispersive signal from the amorphous As overlayer. With increase of $h\nu$, the images gradually develop astonishingly clear dispersive structures formed by the coherent photoelectrons coming from the GaAs underlayer, with their notable shift in angle with $h\nu$ caused by the increase of the transferred p_{ph}. The development reflects weakening of the incoherent photoelectron scattering in the As overlayer with E_k resulting in an increase of photoelectron λ. We note that elastic photoelectron scattering off the As atoms in random positions is also incoherent and forms only a non-dispersive background. By comparison of the experimental images with any band calculations for GaAs one immediately identifies the textbook manifold of the light-hole (LH), heavy-hole (HH) and spin-orbit (SO) split bands, as indicated on the right-hand panel.

Another textbook example is a linear dichroism of the ARPES signal. With our sample and slit orientation the MP coincides with the ΓXU symmetry plane. Fig. 13 shows the ARPES images along the ΓKX directions (with E_k, θ and $h\nu$ now rendered into **k**) measured with different X-ray polarizations. The circular polarization shows up all bands. The *p*-polarization (electric field vector **E** ∥ MP) picks up the HH and SO bands, whereas the *s*-polarization (**E** ⊥ MP) picks up the LH band. The selection rules (see, for example, Hermanson, 1977) immediately identify then the HH and SO states as symmetric and the LH state as antisymmetric relative to the ΓXU plane.

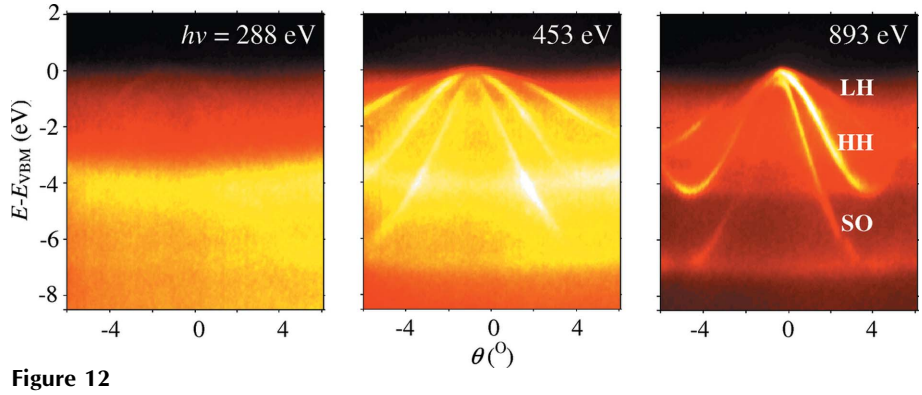

Figure 12
ARPES images acquired on GaAs(100) protected by an amorphous As overlayer with the indicated $h\nu$. Development of the dispersive band structure signal from the GaAs underlayer with increase of $h\nu$ shows the increase of the photoelectron λ (Kobayashi *et al.*, 2012).

Further details of our experiments on GaAs/As can be found by Kobayashi *et al.* (2012). We note that applications of SX-ARPES to samples protected by a capping layer break through the necessity of laborious and, in many cases, destructive procedures to prepare atomically clean surfaces of thin film samples for the ARPES experiment. Samples can be grown in one laboratory (in our case at Tokyo University) and *ex situ* transferred to another one (at SLS) for exhaustive characterization of their native electronic structure with SX-ARPES. This opens new frontiers in diagnostics of electronic devices (such as those based on heterostructures) aimed at optimization of the manufacturing procedures with respect to particular properties of the electronic structure.

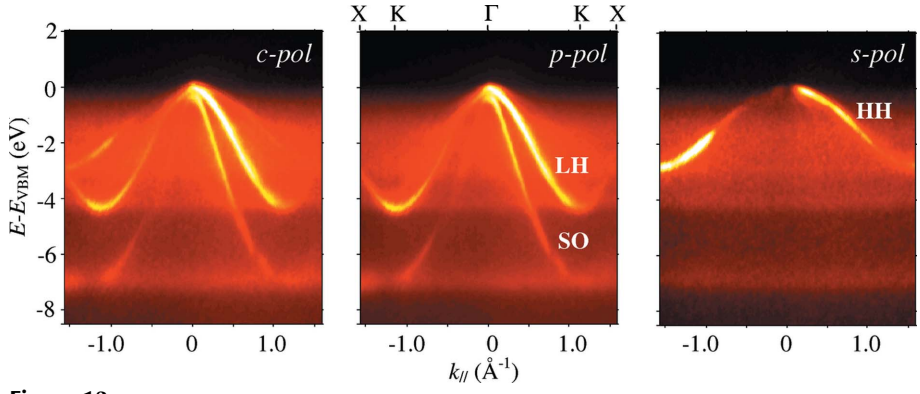

Figure 13
Linear dichroism of GaAs/As in ARPES images along the ΓKX direction measured at $h\nu$ = 892.5 eV with the indicated incident X-ray polarizations. The HH and SO states are symmetric and the LH state is antisymmetric relative to the ΓXU plane.

6.3. Looking resonantly: ferromagnetic impurity band in (Ga,Mn)As

The above method of looking through the As protective layer was applied for investigation of diluted magnetic semiconductor (Ga,Mn)As. This is a paradigm diluted magnetic semiconductor which shows ferromagnetism induced by doped hole carriers. Despite numerous experimental and theoretical investigations, even basic questions about its electronic structure remain open such as the energy position of the Mn 3*d* states in the valence band, and their hybridization with the host GaAs bands (Ohya *et al.*, 2011).

To reveal the Mn 3*d* states in (Ga,Mn)As we have conducted resonant SX-ARPES measurements at the Mn L_3 absorption edge. Our sample had a Mn concentration of only 2.5% which is just above the ferromagnetic transition. Fig. 14(*a*) shows the X-ray absorption spectroscopy (XAS) spectrum which exhibits two peaks at 640 and 640.5 eV. The first peak corresponds to the ferromagnetic substitutional Mn ions, and the second one to the paramagnetic oxidized Mn^{2+} ions segregated in the surface region (Ohe *et al.*, 2009). A series of resonant ARPES images measured with variation of $h\nu$ along the XAS spectrum is shown in Fig. 14(*b*). The image taken at the ferromagnetic XAS peak of 640 eV immediately reveals a Mn 3*d*-derived impurity band (IB) popping up just below E_F. The next ARPES image taken at the paramagnetic XAS peak of $h\nu$ = 640.5 eV shows no more than its afterglow. Therefore, this IB is due to the ferromagnetic Mn ions and, located ∼300 meV below the E_F, induces the ferromagnetism of the charge carriers in (Ga,Mn)As. Further linear dichroism analysis of the resonant spectra, described by Kobayashi *et al.* (2013), reveals significant hybridization of the IB with the LH band of the host GaAs.

This SX-ARPES study has thus immediately resolved the long-disputed ambiguities about the energy position of the IB and its hybridization with the GaAs bands (Ohya *et al.*, 2011; Gray *et al.*, 2012). Its dispersionless character suggests that

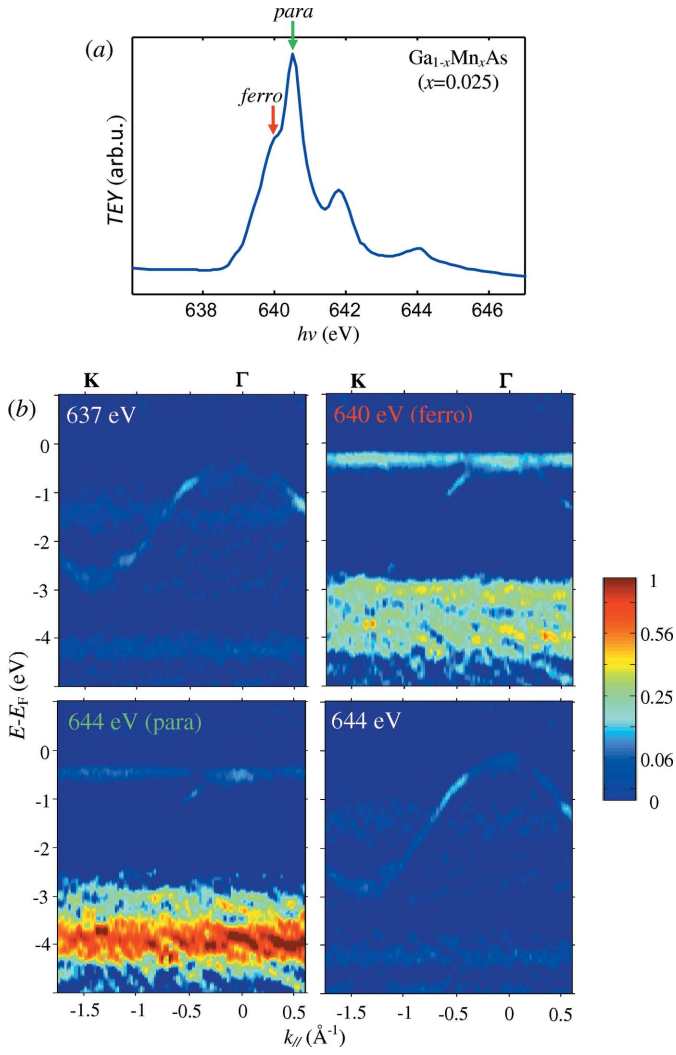

Figure 14
Resonant SX-ARPES at the Mn L_3-edge in (Ga,Mn)As: (*a*) Mn L_3 XAS spectrum, with the arrows showing the ferromagnetic and paramagnetic components; (*b*) ARPES images taken with a few indicated $h\nu$ values across the XAS spectrum with *s*-polarization and represented in negative second derivative $-d^2I/dE^2 > 0$. Tuning $h\nu$ on the ferromagnetic XAS peak at 640 eV immediately reveals the Mn impurity band causing the ferromagnetism of (Ga,Mn)As (Kobayashi *et al.*, 2013).

the (Ga, Mn)As electronic structure should be understood starting from the local Anderson impurity model to describe hybridization of the transition metal *d*-orbitals with the host band electrons. Further details of this study can be found in Kobayashi *et al.* (2013).

7. Comparison of VUV- and SX-ARPES

As a final word, we compare the advantages, weaknesses and main applications of the VUV- and SX-ARPES.

(i) Energy resolution. The state-of-the-art VUV-ARPES is characterized by combined ΔE of the order of a few meV, which allows analysis of low-energy physics such as kinks in the electron dispersions informing of quasiparticle interactions. In contrast, the SX-ARPES figures are up to a few tens of meV, which hides the low-energy physics but allows investigation of physical phenomena of the global valence band energy scale.

(ii) Probing depth. VUV-ARPES is characterized by λ of a few Å, which makes it extremely surface sensitive and limits its applications to atomically clean surfaces. The increase of λ by a few times in SX-ARPES makes it more bulk sensitive and allows applications to real-world systems (such as heterostructures) often without surface preparation.

(iii) Final states and resolution in $k_\perp$. Ill $k_\perp$ definition of the low-energy final states in VUV-ARPES may severely impair reliable investigations of the three-dimensional band dispersions. SX-ARPES solves this problem by virtue of the free-electron-like dispersions and small $k_\perp$ broadening of the final states at higher energies.

(iv) Matrix elements. Complicated matrix-element effects in VUV-ARPES often severely impair data analysis in terms of the spectral function. In contrast, the matrix elements in SX-ARPES are reduced essentially to atomic cross sections with their monotonous energy and **k**-dependence.

(v) Instrumental requirements. Dramatic loss of the valence band Ω in the SX-ARPES energy range makes this technique much more demanding on the flux performance of the synchrotron radiation sources compared with VUV-ARPES. Also higher are requirements on the ARPES analyzer angular resolution.

VUV- and SX-ARPES techniques find, therefore, different and complementary scientific applications. Those of SX-ARPES can be illustrated by numerous research highlights achieved at our facility since the beginning of its operation in early 2011. On top of the above VSe_2, GaAs/As and GaMnAs examples, they include: (i) polarization dependence and alternating FS shapes in three-dimensional pnictide HTSCs, identifying matrix element effects due to intra-cell interference effects; (ii) three-dimensional hybridization effects between *sp*- and *f*-states in heavy-fermion $EuRh_2Si_2$ (Höppner *et al.*, 2013); (iii) topological surface state in the three-dimensional valence band of $PbBi_4Te_7$, with spatial oscillations of its wavefunction reflected by $h\nu$ dependence of ARPES intensity; (iv) three-dimensional electronic structure of an exotic system without inversion symmetry BiTeI (Landolt *et al.*, 2012); (v) electron correlation effects in the bulk of $LaRu_2P_2$ related to the pnictide HTSCs (Razzoli *et al.*, 2012); (vi) FS of buried layers in $LaNiO_3/LaAlO_3$ heterostructures; (vii) depth localization, band structure and FS of two-dimensional electron gas in mixed-valence $LaAlO_3/SrTiO_3$ systems (Cancellieri *et al.*, 2013); (viii) standing X-ray waves excited ARPES of multilayer heterostructures allowing depth-resolved profiling of its electronic structure (Gray *et al.*, 2010), *etc*.

8. Summary

We have presented the concepts and technical realisation of the high-performance SX-ARPES endstation installed at the ADRESS beamline of SLS. The facility operates in the $h\nu$ range from 300 to 1600 eV. Conceptually, the experimental geometry uses a grazing X-ray incidence angle of 20° to increase the photoyield, and the horizontal sample rotation axis to restrict the X-ray footprint on the sample. Technically, the endstation adopts a radial layout of the vacuum chambers to allow most efficient sample manipulation. The high-precision CARVING manipulator delivers three angular DOFs allowing accurate navigation in **k**-space. The sample is liquid-He cooled down to 10.5 K which reduces the incoherent electron–phonon scattering effects to negligible. The rotatable analyzer PHOIBOS-150 is normally used with the parallel slit orientation allowing symmetry analysis of the valence states. Optimization of the MCP bias minimizes the spectral distortions due to the charge spread effects. To align the ARPES spectrometer, we have developed new strategies to match the X-ray beam with the analyzer EFA. This has resulted in a highly accurate angular scale verified through the whole operational energy range. Efficient acquisition and processing of multidimensional ARPES data under variation of $h\nu$ and emission angles uses the software *SmartGUI* based on the concept of vectorized inputs.

The grazing X-ray incidence experimental geometry, fast data acquisition in the fixed mode and, most important, the ADRESS beamline delivering high photon flux above 10^{13} photons s^{-1} (0.01% bandwidth)$^{-1}$ have allowed breakthrough of the dramatic loss of the valence band Ω with energy. Typically, ARPES images of publication quality are delivered in a few minutes. The achieved data acquisition rate has allowed us to extend the SX-ARPES experiment from bulk materials to buried heterostructures and impurities.

Three application examples expose different aspects of the SX-ARPES technique. (i) The ability to explore the three-dimensional electronic structure demonstrated on VSe_2. In addition to high definition of the $k_\perp$ momentum achieved due to increasing photoelectron λ, SX-ARPES benefits from free-electron final states and smooth atomic-like matrix elements. (ii) The ability to access buried interfaces and heterostructures due to increasing λ is demonstrated on As-capped GaAs. (iii) The ability to resonantly excite certain atomic species and explore the elemental composition of the valence states is demonstrated by resolving the Mn impurity band which induces ferromagnetism in (Ga, Mn)As. These examples demonstrate that SX-ARPES with its typical energy resolu-

tion of a few tenths of meV finds applications different and complementary to those of high-resolution VUV-ARPES focused on the quasiparticle interactions. The SX-ARPES keywords are global valence band energy scale, large probing depth, three-dimensional electronic structure, buried heterostructures and impurities, elemental and chemical state specificity, X-ray standing waves, *etc*.

Further information about our SX-ARPES facility including the operation manuals, technical notes as well as data-processing software is available at the ADRESS beamline webpage, http://www.psi.ch/sls/adress/.

APPENDIX *A*
Photon momentum corrections

The geometry of the SX-ARPES experiment at the ADRESS beamline is shown in Fig. 15. The horizontal incident photon beam and analyzer axis form the vertical measurement plane (MP). The analyzer axis is inclined by $\alpha = 20^\circ$. The manipulator axis is horizontal and perpendicular to the MP. The parallel momentum $k_\parallel^x$ is varied through the *primary* manipulator rotation θ_M, and $k_\parallel^y$ through the *tilt* φ_M. The analyzer slit can be oriented either in the MP or perpendicular to it, θ_A and φ_A being the angles along the analyzer slit in these two cases. The origin and sign convention for θ_M, φ_M, θ_A and φ_A are indicated in Fig. 15. Note that with this convention the increase of each of these coordinates increases the corresponding $k_\parallel$.

The photon momentum is calculated as

$$p_{ph} = (2\pi/12400)\,h\nu. \tag{3}$$

Hereinafter the momenta are measured in Å^{-1} and energies in eV.

With our sign convention, the two parallel momentum components of the *initial (photohole) state* can be found as

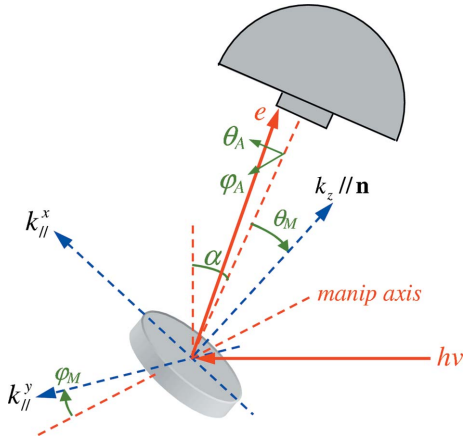

Figure 15
The coordinate system used for the photon momentum correction.

$$k_\parallel^x = 0.5124\,(h\nu - e\phi + E_B)^{1/2}\sin(\theta_A + \theta_M) - 2\pi\,h\nu\cos(\alpha + \theta_M)/12400, \tag{4}$$

$$k_\parallel^y = 0.5124\,(h\nu - e\phi + E_B)^{1/2}\sin(\varphi_A + \varphi_M) + 2\pi\,h\nu\sin(\alpha + \theta_M)\sin\varphi_M/12400, \tag{5}$$

where $e\phi > 0$ is the workfunction, $E_B < 0$ is the binding energy, $\varphi_A = 0$ if the slit is oriented in the MP and $\theta_A = 0$ if perpendicular to it, and θ_M is the surface normal angle relative to the analyzer axis. Note that (i) the second term accounts for p_{ph} and does not depend on the θ_A and φ_A angles along the slit; (ii) owing to rather grazing light incidence in our case the photon momentum correction to $k_\parallel^y$ is small near the normal emission (at $h\nu = 1000$ eV, $\theta_M = 0$ and $\varphi_M = 10^\circ$, for example, the correction is only $\sim$0.03 Å^{-1}) but increases at larger θ_M and φ_M.

For the perpendicular momentum,

$$k_z = 0.5124\left\{h\nu + E_B + V_{000} - 3.81\left[(k_\parallel^x)^2 + (k_\parallel^y)^2\right]\right\}^{1/2} + 2\pi\,h\nu\sin(\alpha + \theta_M)/12400, \tag{6}$$

where $V_{000} > 0$ is the inner potential relative to E_F.

We thank J. H. Dil and C. S. Fadley for valuable discussions, and C. Quitmann, J. F. van der Veen and J. Mesot for their encouragement and continuous support of the SX-ARPES project at SLS. Our thanks extend to T. Kampen and S. Maehl from SPECS GmbH for valuable advice and support of the alignment and operation of the PHOIBOS-150 analyzer.

References

Cancellieri, C., Reinle-Schmitt, M. L., Kobayashi, M., Strocov, V. N., Schmitt, T. & Willmott, P. R. (2013). *Phys. Rev. Lett.* **110**, 137601.
Fadley, C. S., Yang, S.-H., Mun, B. S. & Garcia de Abajo, F. J. (2003). *Solid-State Photoemission and Related Methods: Theory and Experiment*, edited by W. Schattke and M. A. Van Hove, pp. 404–432. Berlin: Wiley-VCH.
Gray, A. X., Minár, J., Ueda, S., Stone, P. R., Yamashita, Y., Fujii, J., Braun, J., Plucinski, L., Schneider, C. M., Panaccione, G., Ebert, H., Dubon, O. D., Kobayashi, K. & Fadley, C. S. (2012). *Nat. Mater.* **11**, 957.
Gray, A. X., Papp, C., Balke, B., Yang, S.-H., Huijben, M., Rotenberg, E., Bostwick, A. A., Ueda, S., Yamashita, Y., Kobayashi, K., Gullikson, E. M., Kortright, J. B., DeGroot, F. M. F., Rijnders, G., Blank, D. H. A., Ramesh, R. & Fadley, C. S. (2010). *Phys. Rev. B*, **82**, 205116.
Gray, A. X., Papp, C., Ueda, S., Balke, B., Yamashita, Y., Plucinski, L., Minár, J., Braun, J., Ylvisaker, E. R., Schneider, C. M., Pickett, W. E., Ebert, H., Kobayashi, K. & Fadley, C. S. (2011). *Nat. Mater.* **10**, 759.
Henke, B. L. (1972). *Phys. Rev. A*, **6**, 94–104.
Henke, B. L., Gullikson, E. M. & Davis, J. C. (1993). *At. Data Nucl. Data Tables*, **54**, 181 (http://henke.lbl.gov/optical_constants/).
Hermanson, J. (1977). *Solid State Commun.* **22**, 9–11.
Höppner, M., Seiro, S., Chikina, A., Fedorov, A., Güttler, M., Danzenbächer, S., Generalov, A., Kummer, K., Patil, S., Molodtsov, S. L., Kucherenko, Y., Geibel, C., Strocov, V. N., Shi, M., Radovic, M., Schmitt, T., Laubschat, C. & Vyalikh, D. V. (2013). *Nat. Commun.* **4**, 1646.

Hüfner, S. (1996). *Photoelectron Spectroscopy: Principles and Applications.* Berlin: Springer.
Kobayashi, M., Iriya, M., Takeda, Y., Fujimori, A., Schmitt, T., Patthey, L., Ohya, S., Tanaka, M., Oshima, M., Strocov, V. N. (2013). Available at http://arxiv.org/abs/1302.0063.
Kobayashi, M., Muneta, I., Schmitt, T., Patthey, L., Ohya, S., Tanaka, M., Oshima, M. & Strocov, V. N. (2012). *Appl. Phys. Lett.* **101**, 242103.
Landolt, G., Eremeev, S. V., Koroteev, Y. M., Slomski, B., Muff, S., Neupert, T., Kobayashi, M., Strocov, V. N., Schmitt, T., Aliev, Z. S., Babanly, M. B., Amiraslanov, I. R., Chulkov, E. V., Osterwalder, J. & Dil, J. H. (2012). *Phys. Rev. Lett.* **109**, 116403.
Maehl, S. (2012). Private communication.
Månsson, M., Claesson, T., Pailhés, S., Chang, J., Mesot, J., Shi, M., Patthey, L., Momono, N., Oda, M., Ido, M., Karlsson, U. O. & Tjernberg, O. (2007). *Rev. Sci. Instrum.* **78**, 076103.
Mårtensson, N., Baltzer, P., Brühwiler, P. A., Forsell, J.-O., Nilsson, A., Stenborg, A. & Wannberg, B. (1994). *J. Electron Spectrosc. Relat. Phenom.* **70**, 117–128.
Ohe, J.-I., Tomoda, Y., Bulut, N., Arita, T., Nakamura, K. & Maekawa, S. (2009). *J. Phys. Soc. Jpn*, **78**, 083703.
Ohya, S., Takata, K. & Tanaka, M. (2011). *Nat. Phys.* **7**, 342.
Patthey, L. (2010). Private communication.
Powell, C. J., Jablonski, A., Tilinin, I. S., Tanuma, S. & Penn, D. R. (1999). *J. Electron Spectrosc. Relat. Phenom.* **98/99**, 1–15.
Razzoli, E., Kobayashi, M., Strocov, V. N., Delley, B., Bukowski, Z., Karpinski, J., Plumb, N. C., Radovic, M., Chang, J., Schmitt, T., Patthey, L., Mesot, J. & Shi, M. (2012). *Phys. Rev. Lett.* **108**, 257005.
Schmitt, T., Strocov, V. N., Zhou, K., Schlappa, J., Monney, C., Flechsig, U. & Patthey, L. (2013). *J. Electron Spectrosc. Relat. Phenom.*, doi:10.1016/j.elspec.2012.12.011.
Sekiyama, A., Kasai, S., Tsunekawa, M., Ishida, Y., Sing, M., Irizawa, A., Yamasaki, A., Imada, S., Muro, T., Saitoh, Y., Onuki, Y., Kimura, T., Tokura, Y. & Suga, S. (2004). *Phys. Rev. B.* **70**, 060506(R).
Solterbeck, C., Schattke, W., Zahlmann-Nowitzki, J.-W., Gawlik, K.-U., Kipp, L., Skibowski, M., Fadley, C. S. & Van Hove, M. A. (1997). *Phys. Rev. Lett.* **79**, 4681–4684.
Strocov, V. N. (2003). *J. Electron Spectrosc. Relat. Phenom.* **130**, 65–78.
Strocov, V. N. (2013). *J. Synchrotron Rad.* **20**, 517–521.
Strocov, V. N., Krasovskii, E. E., Schattke, W., Barrett, N., Berger, H., Schrupp, D. & Claessen, R. (2006). *Phys. Rev. B*, **74**, 195125.
Strocov, V. N., Schmitt, T., Flechsig, U., Schmidt, T., Imhof, A., Chen, Q., Raabe, J., Betemps, R., Zimoch, D., Krempasky, J., Wang, X., Grioni, M., Piazzalunga, A. & Patthey, L. (2010). *J. Synchrotron Rad.* **17**, 631–643.
Strocov, V. N., Shi, M., Kobayashi, M., Monney, C., Wang, X. Q., Krempasky, J., Schmitt, T., Patthey, L., Berger, H. & Blaha, P. (2012). *Phys. Rev. Lett.* **109**, 086401.
Strocov, V. N., Starnberg, H. I., Nilsson, P. O., Brauer, H. E. & Holleboom, L. J. (1997). *Phys. Rev. Lett.* **79**, 467–470.
Suga, S., Shigemoto, A., Sekiyama, A., Imada, S., Yamasaki, A., Irizawa, A., Kasai, S., Saitoh, Y., Muro, T., Tomita, N., Nasu, K., Eisaki, H. & Ueda, Y. (2004). *Phys. Rev. B*, **70**, 155106.
Taylor, R. C., Hettrick, M. C. & Malina, R. F. (1983). *Rev. Sci. Instrum.* **54**, 171.
Terashima, K., Sato, T., Komatsu, H., Takahashi, T., Maeda, N. & Hayashi, K. (2003). *Phys. Rev. B*, **68**, 155108.
Venturini, F., Minár, J., Braun, J., Ebert, H. & Brookes, N. B. (2008). *Phys. Rev. B*, **77**, 045126.
Wannberg, B. (2009). *Nucl. Instrum. Methods Phys. Res. A*, **601**, 182–194.
Woolley, A. M. & Wexler, G. (1977). *J. Phys. C*, **10**, 2601.
Yeh, J. J. & Lindau, I. (1985). *At. Data Nucl. Data Tables*, **32**, 1 (http://ulisse.elettra.trieste.it/services/elements/WebElements.html).